Contemporary Mathematics
https://ojs.wiserpub.com/index.php/CM/

Research Article

Rapid Quantification of CEST Parameters Based on Multi-Starting Point Optimization and Bloch-Mcconnell Analytical Solution

Gang Xiao[1], Zhen Cao[2], Tingting Nie[3], Caiyu Zhuang[4], Yuhong Lu[5,6], Renhua Wu[6*], Xiaolei Zhang[6*]

[1] School of Mathematics and Statistics, Hanshan Normal University, Chaozhou 521041, China
[2] Department of Radiology, Fengshun County People's Hospital, Meizhou 514300, China
[3] Department of Radiology, Hubei Cancer Hospital, Tongji Medical College, Huazhong University of Science and Technology, Wuhan 430079, China
[4] Department of Radiology, First Affiliated Hospital of Shantou University Medical College, Shantou 515041, China
[5] College of Engineering, Shantou University, Shantou 515063, China
[6] Department of Radiology, Second Affiliated Hospital of Shantou University Medical College, Shantou 515041, China
E-mail: rhwu@stu.edu.cn (R.W.); xlzhang_nathan@stu.edu.cn (X.Z.)

Received: 27 October 2025; **Revised:** 16 January 2026; **Accepted:** 9 March 2026

Abstract: This study presents an innovative approach that combines multi-start (MS) optimization with the Bloch-McConnell eigenspace analytical solution for the rapid and accurate quantification of chemical exchange saturation transfer parameters. The core advantage of this method lies in the global search capability of the MS algorithm, which reduces the reliance on a single initial value and mitigates the risk of getting trapped in local optima, a common issue with traditional fitting methods. Additionally, by utilizing the exchange-dependent relaxation rate in the rotating frame, the computational process is simplified, significantly enhancing the stability and reliability of parameter estimation. Simulation results show that, compared to traditional optimization methods such as genetic algorithms, particle swarm optimization, and global search algorithms, our method reduces computation time from 9358.9 seconds to 2175.1 seconds, achieving a 4.3-fold acceleration while maintaining lower reconstruction errors. A 7 T magnetic resonance imaging (MRI) rat brain experiment validated the robustness of this method under different B_1 field conditions, and the generated high-resolution parameter maps accurately distinguish tumor from normal tissue, demonstrating the potential of this method for real-time chemical exchange saturation transfer (CEST) imaging. By reducing computation time and improving accuracy, this method provides an efficient and reliable tool for clinical and research applications.

***Keywords*:** chemical exchange saturation transfer, Z-spectra, parameter quantification, R_{ex}-line-fit, multi-start algorithm

MSC: 65K10, 68U10, 92C55

1. Introduction

Chemical exchange saturation transfer (CEST) magnetic resonance imaging (MRI) is an increasingly prominent technique in molecular imaging, offering valuable insights into molecular compound detection and focal pathologies [1–8]. By providing contrast at the molecular and metabolic levels, CEST enables the indirect detection of solute protons

DOI: https://doi.org/10.37256/cm.7420269007

exchanging with water protons. Notably, quantitative CEST methods have the potential to address the challenges associated with quantifying CEST effects, offering greater precision in molecular imaging [7].

In clinical settings, the ability to process and analyze CEST data rapidly is crucial. The development of efficient and accurate quantitative CEST methods holds particular promise for clinical applications, particularly in enabling real-time analysis of large datasets—an essential requirement for many diagnostic and therapeutic procedures. However, current methods for quantifying CEST parameters often involve lengthy computational processes, limiting their practical utility in time-sensitive clinical environments.

Traditionally, the Bloch-McConnell (BM) equations have been fundamental in modeling the complex dynamics of precession, relaxation, and exchange within multi-pool systems. These equations have provided a theoretical framework for quantifying CEST parameters by fitting Z-spectra. However, the application of BM equations in quantitative analysis is not without its challenges: (1) Computational Complexity: Solving the BM equations numerically requires significant computational resources and time, which can limit their utility in clinical settings [9]; (2) Local Optima: Common optimization methods for solving the BM equations often fall into local optima, failing to find the global solution [10, 11]; (3) Sensitivity to Initial Conditions: The success of these methods is heavily influenced by the selection of initial values, which can lead to variability in results [10]. Furthermore, the computational burden imposed by these numerical methods limits the practical utility of CEST MRI in time-sensitive clinical settings. Z-spectra fitting, integral to parameter quantification, requires optimization algorithms that often struggle with the computational demands and challenges posed by noise and initial value selection.

In recent years, various strategies have been proposed to address these issues. Shah and colleagues explored optimization methods to improve Z-spectra fitting [9]; however, these methods still faced challenges related to computational demands. Carradus et al. applied particle swarm optimization (PSO) to refine parameter estimation, but their approach still struggled with local optima and required considerable computational resources [11]. PSO demonstrated improvements over traditional methods, but it remained computationally intensive and prone to settling on suboptimal solutions. Wen et al. highlighted the critical importance of selecting appropriate initial values, showing that poor starting points often resulted in subpar or erroneous estimates [10]. These challenges underscore the need for more efficient, robust approaches for quantitative CEST analysis.

This study introduces a novel approach that combines multi-start (MS) optimization with the BM eigenspace analytical solution to address the primary challenges in CEST quantification. The MS algorithm enhances the optimization process by generating multiple random starting points, reducing the reliance on a single initial value, and mitigating the risk of getting trapped in local optima. This global search capability significantly improves the robustness of the solution and ensures a more reliable optimization process. This approach, which has been validated in previous works [12, 13], ensures a more comprehensive exploration of the solution space, leading to better optimization outcomes. Additionally, by utilizing the exchange-dependent relaxation rate (R_{ex}) in the rotating frame, the proposed method bypasses the need for computationally expensive numerical integration of the BM equations. The R_{ex} parameter, which depends on specific variables such as solute concentration, exchange rate, and transverse relaxation time, enables a more accurate and computationally efficient quantification of CEST parameters [6, 8, 14].

The combination of MS optimization and the BM eigenspace solution provides a more efficient framework for CEST quantification. Simulation results demonstrate that this method accelerates computation time by over four times compared to traditional optimization techniques, such as genetic algorithms (GA), PSO, and global search (GS) algorithms. Specifically, the computation time is reduced from 9358.9 seconds to 2175.1 seconds, while maintaining lower reconstruction errors. In vivo validation of the method using 7 T MRI rat brain scans confirms its robustness under varying B_1 field conditions and demonstrates its capability to distinguish tumor tissue from normal tissue with high-resolution parameter maps. This validation underscores the potential of this method for real-time CEST imaging, where rapid and accurate parameter quantification is crucial for clinical decision-making.

In summary, the proposed method presents a significant advancement in CEST MRI, offering a faster, more reliable tool for quantitative analysis. By combining MS optimization with the BM eigenspace analytical solution, we provide a comprehensive framework that reduces computational time, improves parameter estimation accuracy, and enhances the clinical applicability of CEST imaging. This approach holds great promise for advancing the role of CEST MRI in both

clinical diagnostics and biomedical research, particularly in the context of personalized medicine, real-time monitoring, and early detection of pathologies.

The remainder of the paper is organized as follows: Section 2 discusses the theoretical foundation of the BM eigenspace solution and MS optimization, emphasizing the advantages of optimizing initial conditions and overcoming noise-induced challenges. Section 3 outlines the experimental design, including simulation setups and in vivo protocols for testing the method. Section 4 presents the results from these experiments, highlighting the improvements in CEST quantification accuracy and efficiency. Section 5 explores the potential clinical implications, addressing the broader impact of the method on healthcare applications, while Section 6 concludes with a summary of findings and future research directions.

2. Theory

2.1 *BM eigenspace analytical solution—the exchange-dependent relaxation rate in the rotating frame*

The BM eigenspace analytical solution, which incorporates the exchange-dependent relaxation rate in the rotating frame (R_{ex}), offers a computationally efficient approach for fitting Z-spectra. The Z-spectra, defined as the normalized Z-magnetization $Z(\Delta\omega) = \frac{M_{sat}(\Delta\omega)}{M_0}$ at each saturation offset $\Delta\omega$, can be modeled using a monoexponential decay equation [14]:

$$Z(\Delta\omega) = Z_i \cdot e^{-R_{1,\rho} \cdot t_{sat}} + Z^{ss} \cdot \left(1 - e^{-R_{1,\rho} \cdot t_{sat}}\right) \tag{1}$$

where $Z_i = \frac{\|M_i\|}{M_0}$ represents the initial Z-magnetization, t_{sat} is the saturation time, and Z^{ss} is the steady-state magnetization, which is given by [15]:

$$Z^{ss} = \frac{R_{1,w} \cdot \cos^2\theta}{R_{1,\rho}} \tag{2}$$

where $\theta = \tan^{-1}\left(\frac{\omega_1}{\Delta\omega}\right)$ is the effective tilt angle in the rotating frame, $\omega_1 = \gamma B_1$ is the amplitude of the RF field.

In the case of a two-pool system, where one pool represents water, the relaxation rate $R_{1,\rho}$ is the sum of R_{eff} (the water proton relaxation rate in the rotating frame) and R_{ex} (the exchange-dependent relaxation rate):

$$R_{1,\rho} = R_{eff} + R_{ex} \tag{3}$$

The term R_{eff}, which is the relaxation rate for water, can be approximated by:

$$R_{eff} = R_{1,w}\cos^2\theta + R_{2,w}\sin^2\theta \tag{4}$$

Where $R_{1,w}$ and $R_{2,w}$ represent the longitudinal and transverse relaxation rates of water, respectively.

The exchange-dependent relaxation rate R_{ex} for a given pool i at an off-resonant frequency $\Delta\omega$ is given by the following analytical expression [16]:

$$R_{ex,\,i}(\Delta\omega) = f_i \cdot k_i \cdot \frac{\omega_1^2}{\omega_1^2 + k_i^2 + (\Delta\omega - \Delta_i)^2 + \frac{k_i^2 \cdot R_{2,\,i}^2}{k_i^2 + (\Delta\omega - \Delta_i)^2}} \tag{5}$$

where f_i is the fraction of protons in pool i, k_i is the exchange rate with water (Hz), $R_{2,i}$ is the transverse relaxation rate (Hz), Δ_i is the chemical shift difference between pool i and water (ppm).

For a multi-pool system with direct saturation (pool w) and multiple exchanging pools (pools i), the relaxation rates in the rotating frame contribute additively to the global rate

$$R_{1,\rho} = R_{\text{eff}} + \sum_i R_{\text{ex},\,i},\ \ i = 1, 2, \ldots, N \tag{6}$$

2.2 *Multi-start method*

The original multi-start procedures were developed as a means to leverage a local or neighborhood search algorithm by implementing it across multiple random initial solutions, and modern multi-start methods typically integrate a robust diversification approach in solution generation to effectively combat local optimality [12].

Consider a finite ground set E, a set of feasible solutions $F \subseteq 2^E$, and an objective function f: $2^E \to \mathbb{R}$. In the minimization version, we search an optimal solution $S^* \in F$ such that $f(S^*) \leqslant f(S)$, $\forall S \in F$. The ground set E, the cost function f, and the set of feasible solutions F are defined for each specific problem. A basic multi-start procedure simply applies procedure ConstructSolution multiple times, returning the best solution found over all starts. The procedures ConstructSolution and MultiStart are illustrated in **Algorithm 1** and **Algorithm 2** [13], respectively.

Algorithm 1 ConstructSolution

Step 1: Initialize the solution set S as empty ($S \leftarrow \emptyset$).
Step 2: Define a candidate set C, which consists of all elements $s \in E$ such that $S \cup \{s\}$ is not infeasible.
Step 3: Enter a loop that continues as long as $C \neq \emptyset$.
Step 4: Select an element $s \in C$ and add it to the solution set S. (Update $S \leftarrow S \cup \{s\}$).
Step 5: Update the candidate set C to include all elements $s \in E$ such that $S \cup \{s\}$ is not infeasible.
Step 6: Repeat Steps 4–5 until the loop ends (when $C = \emptyset$).
Step 7: Return the final solution set S.

Algorithm 2 MultiStart

Step 1: Initialize the best solution value f^* to infinity ($f^* \leftarrow \infty$).
Step 2: Enter a loop that continues until a stopping criterion is met.
Step 3: Construct a feasible solution S by calling the ConstructSolution procedure.
Step 4: If the objective value of the solution $f(S)$ is less than the current best f^*, then update the best solution S^* and the best value f^* with S and $f(S)$, respectively.
Step 5: Repeat Steps 3–4 until the stopping criterion is satisfied.
Step 6: Return the best solution S^*.

2.3 *Multi-start R_{ex}-line-fit*

To ensure the reproducibility and methodological clarity of the proposed framework, it is necessary to explicitly describe how the multi-start strategy is implemented in practice, particularly with respect to the stopping criteria and the

selection of the final solution. Although the advantage of using multiple initializations lies in reducing sensitivity to initial values, the convergence behavior of the algorithm is also governed by the local optimization steps and their stopping conditions.

In this work, all initial starting points are treated independently and are subject to identical local stopping criteria, while the final solution is determined through a global selection rule across all candidate solutions. To clearly illustrate this two-level optimization procedure—namely, single-start local optimization followed by multi-start global selection—we summarize the complete multi-start R_{ex}-line-fit workflow in **Algorithm 3**.

Algorithm 3 Multi-start R_{ex}-line-fit

Input:

Z-spectra $\mathbf{Z}_{meas}$; R_{ex} model $\mathbf{Z}_{model}(\mathbf{x})$;
parameter bounds [lb, ub]; number of starts N.

Output:

Optimal parameter estimate $\widehat{\mathbf{x}}$.

1. Generate N initial points $\{\mathbf{x}_0^{(k)}\}_{k=1}^{N}$ within [lb, ub] (MultiStart with StartPointsToRun = 'bounds').
2. **For each starting point** $k = 1, \ldots, N$:

- Independently solve:

$$\min_{\mathbf{x}} \|\mathbf{Z}_{meas} - \mathbf{Z}_{model}(\mathbf{x})\|_2^2$$

using lsqnonlin.

- Terminate the local optimization if **any** of the following holds:

(i) change in objective function below tolerance;
(ii) change in parameters below tolerance;
(iii) maximum number of iterations reached.

- Store the candidate solution $\widehat{\mathbf{x}}^{(k)}$ and its residual.

3. Select the solution with the minimum residual among all candidates:

$$\widehat{\mathbf{x}} = \arg\min_{k} f\left(\widehat{\mathbf{x}}^{(k)}\right).$$

Note: Stopping criteria are evaluated **independently for each start**; convergence of all starts to the same solution is not required; the final estimate is determined by a **best-of-all** selection rule.

3. In vivo MR imaging

All animal handling and experimental protocols were performed in accordance with the National Research Council's Guide for the Care and Use of Laboratory Animals. The study protocols involving animals received approval from the Ethics Committee of Shantou University Medical College (Approval No. SUMCXM2024-165), and all procedures were carried out following the animal research: reporting of in vivo experiments (ARRIVE) guidelines. The MR imaging of Sprague-Dawley rats is detailed in Appendix.

4. Results

4.1 *Simulation*

To validate the performance of the proposed approach, simulated Z-spectra are created using multi-pool R_{ex} system, and the solute pool parameters with lower bounds (LB) and upper bounds (UB) are listed in Table 1. For water pool, the $T_{1,w}$ with LB = 1 s and UB = 4 s, and $T_{2,w}$ with LB = 0.02 s and UB = 0.1 s, are considered. For each pool parameter, the 1297 variables are randomly selected in the normal distribution between the LB and UB, thus yielding 1297 simulated Z-spectra. To allow comparison between MS and standard optimization algorithm, the R_{ex} fitting is conducted by using MS [12, 13], genetic algorithm (GA) [17], PSO [18] and global search (GS) [19], respectively.

Table 1. Summary of the parameters for a general exchanging pool i when we conduct R_{ex}-line-fit: solute-water exchange rate (k_i), solute concentration (f_i), transverse relaxation time ($T_{2,s}$), and solute resonance frequency offset (Δ)

		Amide	Guanidino	MT	NOE
k_s (s^{-1})		1∼250	1∼1000	1∼50	1∼100
f_s (10^{-3})	LB∼ UB	1∼10	0.1∼10	10∼1000	1∼10
$T_{2,s}$ (10^{-3} s)		0.1∼10	1∼20	0.01∼0.3	0.1∼10
Δ (ppm)	3.5	2.0	−2.3	−3.5	

Note: MT: Magnetization Transfer; NOE: Nuclear Overhauser Effect

In addition, Table 2 lists the parameters of GA, PSO, GS and MS when they are applied to solve the solution of CEST parameters in simulation.

Table 2. Comparison of optimization methods: parameters and execution time

Algorithm	Key Parameters	Execution Time in Our Simulation
Genetic algorithm (GA)	Population size Generations Chromosome length Fitness evaluation time	4173.2 s
Particle swarm optimization (PSO)	Swarm size Iterations Dimension Fitness evaluation time	2949.5 s
Global search	Number of local searches Single local search time	9358.9 s
Multi-start	Number of starting points Single local search time	2175.1 s

We first applied the four optimization algorithms (GA, PSO, GS and MS) to solve the solution of CEST parameters. Figure 1 illustrates the mean reconstructed errors when GA, PSO, GS and MS are applied to solve the solution of CEST parameters ($T_{2,s}$, k_s and f_s). Clearly, our MS exhibits best results.

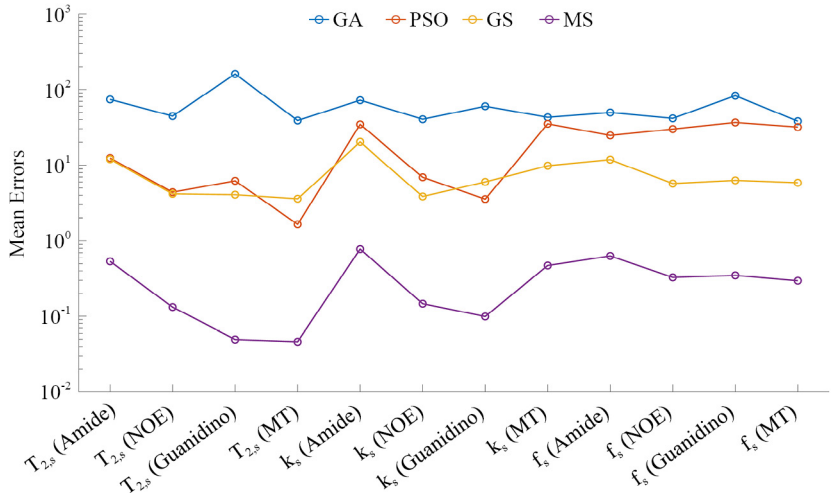

Figure 1. The mean reconstructed errors when GA, PSO, GS and MS are applied to solve the solution of considered CEST parameters ($T_{2,s}$, k_s and f_s)

4.2 *In vivo*

A. Performance of MS algorithm without singular value decomposition (SVD) denoising

Herein, we evaluated the in vivo performance of the MS algorithm using 1000 starting points without SVD denoising. We first conduct an experiment of parameter imaging (solute transverse relaxation $T_{2,s}$, solute-water exchange rate k_s, solute concentration f_s) for Amide at 3.5 ppm, NOE at −3.5 ppm, Guanidino at 2.0 ppm, and MT at −2.3 ppm. Figure 2 illustrates the parameter imaging of these CEST effects by MS algorithm. The region of pseudo color image overlaid on anatomy image is the region of interest (ROI).

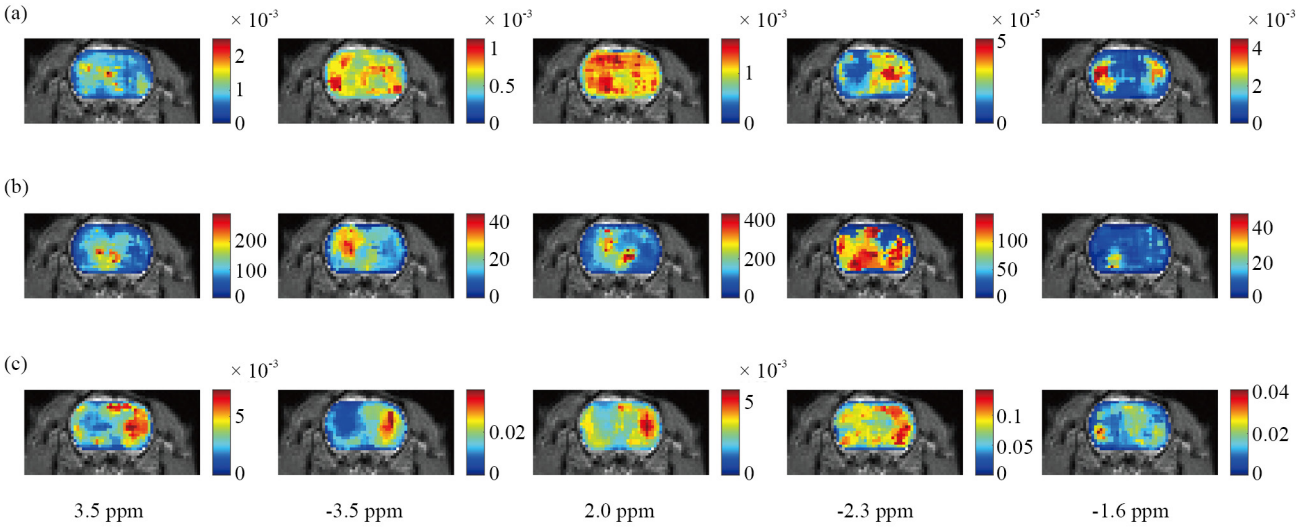

Figure 2. The parameter imaging of Amide at 3.5 ppm, NOE at −3.5 ppm, Guanidino at 2.0 ppm, and MT at −2.3 ppm when we apply MS algorithm to solve the solution of CEST parameters. (a) Imaging of solute transverse relaxation $T_{2,s}$, (b) Imaging of solute-water exchange rate k_s, (c) Imaging of solute concentration f_s

Figure 3 illustrates the Z-spectra fitting from the tumor region (left red contour line) and the contralateral region (right red contour line) under three B_1 values (B_1 = 0.6 μT, B_1 = 1.0 μT, B_1 = 1.6 μT) using the R_{ex}-line-fit that solved

by MS using 1000 starting points without SVD denoising. The results show that the satisfied accuracy and consistency are obtained by the R_{ex}-line-fit when it is solved by MS, and it displays great agreement and follows the same tendency as the actual measurements around 3.5, 2.0, -3.5 and -2.3 ppm. The corresponding Z-spectra fitting results of the MS algorithm using 50 and 100 starting points without SVD denoising are illustrated in Figure A1 and Figure A2 of Appendix.

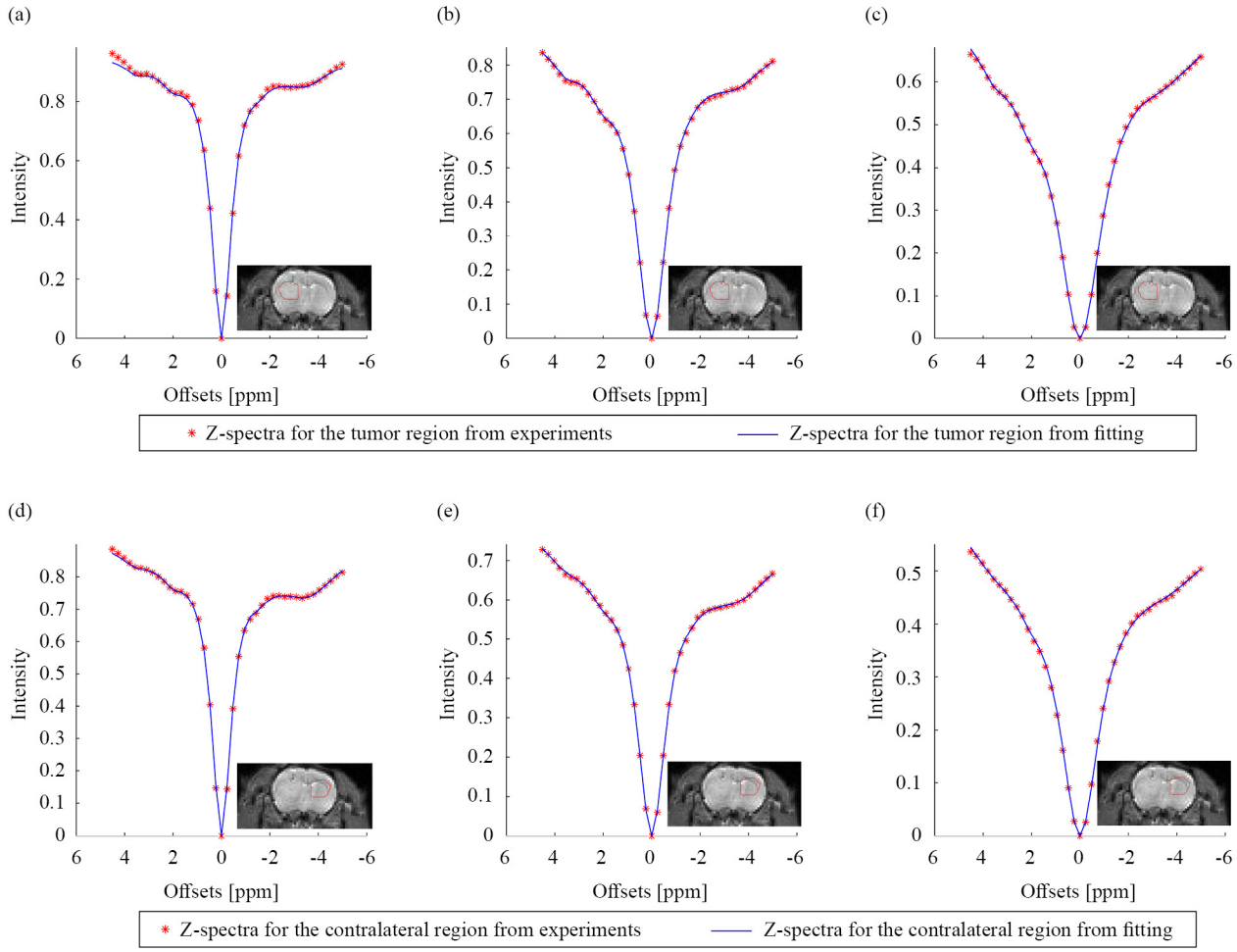

Figure 3. Z-spectra fitting from the tumor region and the contralateral region using the R_{ex}-line-fit when it is solved by MS using 1000 starting points without SVD denoising. (a) $B_1 = 0.6\ \mu$T for the tumor region, (b) $B_1 = 1.0\ \mu$T for the tumor region, (c) $B_1 = 1.6\ \mu$T for the tumor region, (d) $B_1 = 0.6\ \mu$T for the contralateral region, (e) $B_1 = 1.0\ \mu$T for the contralateral region, (f) $B_1 = 1.6\ \mu$T for the contralateral region

In this section, we conduct ablation experiments and sensitivity analysis to comprehensively evaluate the in vivo performance of the proposed method. Considering that noise in the Z-spectra leads to a reduced signal-to-noise ratio (SNR) in vivo, we first provide the Z-spectra fitting from the tumor region (left red contour line) and the contralateral region (right red contour line) under three B_1 values ($B_1 = 0.6\ \mu$T, $B_1 = 1.0\ \mu$T, $B_1 = 1.6\ \mu$T) using the R_{ex}-line-fit that solved by MS using 1000 starting points with SVD denoising (Figure 4). The corresponding Z-spectra fitting results of the MS algorithm using 50 and 100 starting points with SVD denoising are illustrated in Figure A3 and Figure A4 of Appendix.

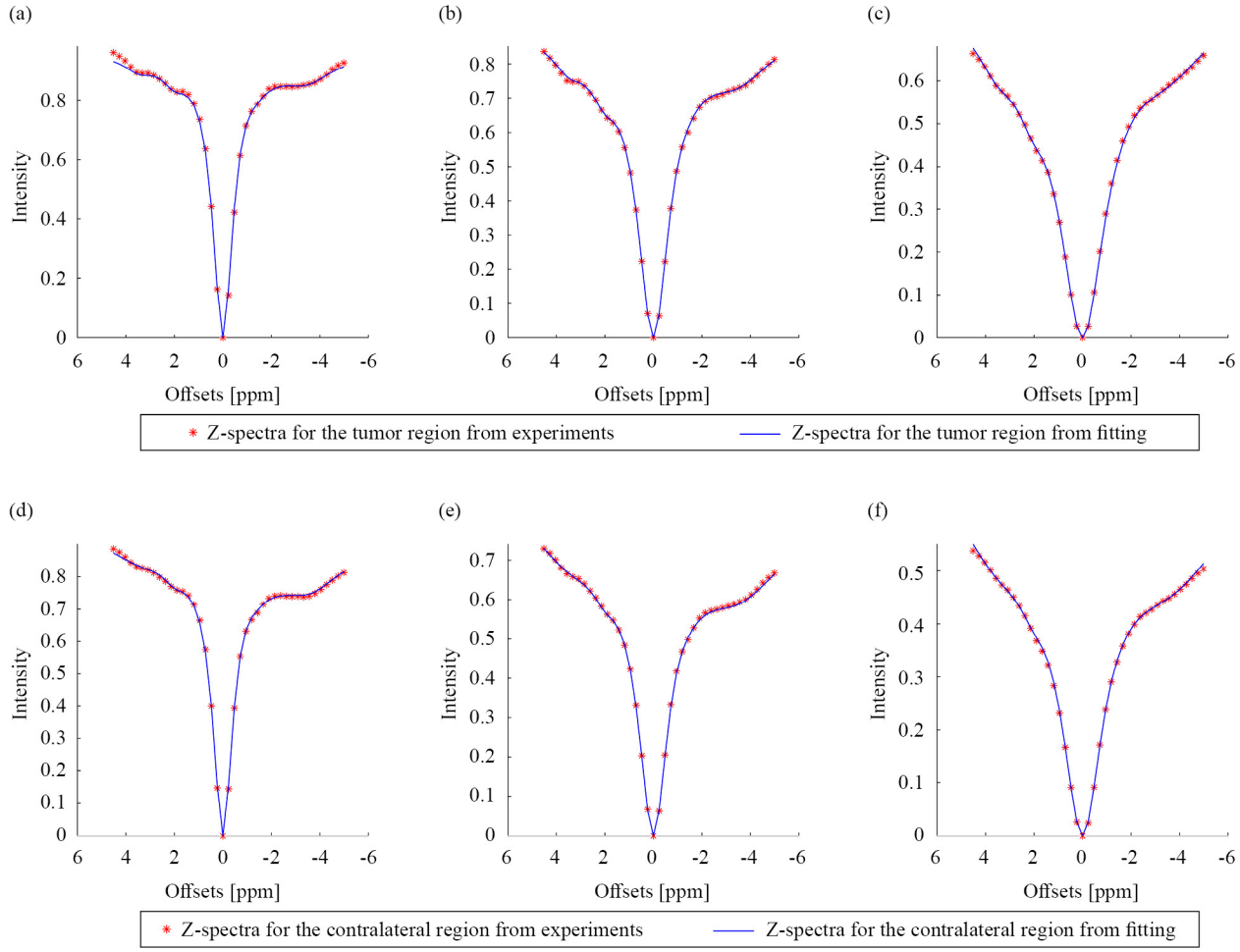

Figure 4. Z-spectra fitting from the tumor region and the contralateral region using the R_{ex}-line-fit when it is solved by MS using 1000 starting points with SVD denoising. (a) $B_1 = 0.6\ \mu$T for the tumor region, (b) $B_1 = 1.0\ \mu$T for the tumor region, (c) $B_1 = 1.6\ \mu$T for the tumor region, (d) $B_1 = 0.6\ \mu$T for the contralateral region, (e) $B_1 = 1.0\ \mu$T for the contralateral region, (f) $B_1 = 1.6\ \mu$T for the contralateral region

Subsequently, two validation experiments were conducted to further assess the robustness and reliability of the proposed method. In the first experiment, the MS algorithm was directly applied to perform R_{ex}-line-fit (Table 3). In the second experiment, SVD was employed to denoise the Z-spectra prior to R_{ex}-line-fit (Table 4). In addition, to assess the sensitivity of the multi-start algorithm to the number of initial starting points, three configurations were investigated in each experiment, with the number of starting points set to 50, 100, and 1000, respectively.

Table 3. Quantitative in vivo R_{ex}-line-fit performance of the multi-start algorithm by root mean square error (RMSE)

Regions	Tumor region			Contralateral region		
Number of starting points	50	100	1000	50	100	1000
$B_1 = 0.6\ \mu$T	0.01729	0.01722	0.01719	0.00794	0.00793	0.00787
$B_1 = 1.0\ \mu$T	0.00532	0.00502	0.00499	0.00450	0.00439	0.00435
$B_1 = 1.6\ \mu$T	0.00646	0.00707	0.00706	0.01030	0.01014	0.01049

Table 4. Quantitative in vivo R_{ex}-line-fit performance with SVD-denoised Z-spectra by root mean square error (RMSE)

Regions	Tumor region			Contralateral region		
Number of starting points	50	100	1000	50	100	1000
$B_1 = 0.6\ \mu$T	0.01661	0.01664	0.01660	0.00750	0.00739	0.00740
$B_1 = 1.0\ \mu$T	0.00531	0.00519	0.00510	0.00510	0.00515	0.00510
$B_1 = 1.6\ \mu$T	0.00612	0.00645	0.00656	0.01087	0.01120	0.01145

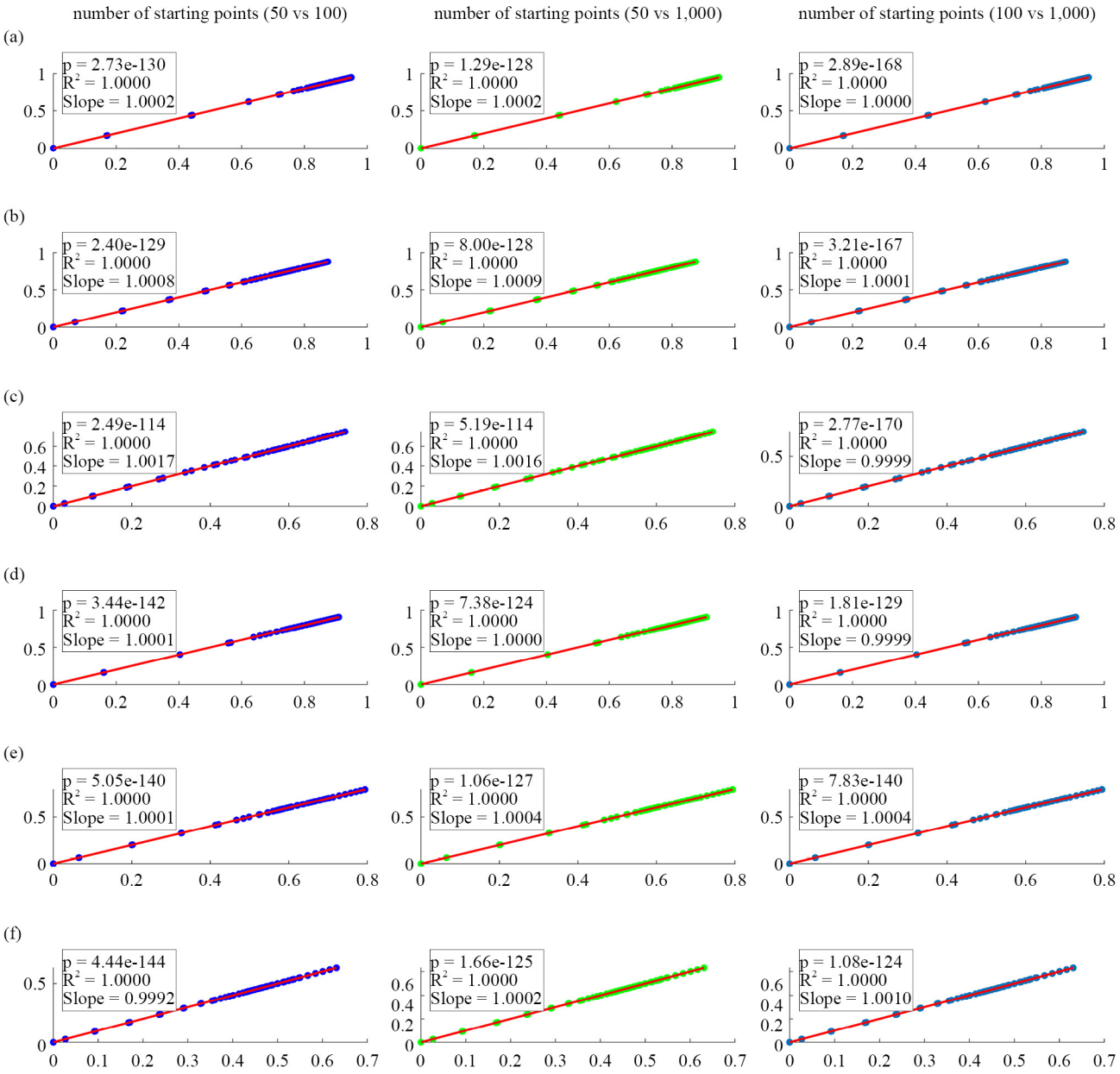

Figure 5. Linear regression analysis of Z-spectra fitting results obtained with different numbers of starting points (50, 100, and 1000) and B_1 values (0.6 μT, 1.0 μT, and 1.6 μT) in the tumor and contralateral regions. (a): $B_1 = 0.6\ \mu$T for the tumor region; (b): $B_1 = 1.0\ \mu$T for the tumor region; (c): $B_1 = 1.6\ \mu$T for the tumor region; (d): $B_1 = 0.6\ \mu$T for the contralateral region; (e): $B_1 = 1.0\ \mu$T for the contralateral region; (f): $B_1 = 1.6\ \mu$T for the contralateral region

The experimental results demonstrate that: (1) the proposed method exhibits strong robustness against noise, as reflected by the comparable root mean square error (RMSE) values obtained with and without SVD-based denoising; and (2) the multi-start algorithm used in the proposed framework is insensitive to the number of starting points, yielding similar RMSE values across different initializations (50, 100, and 1000).

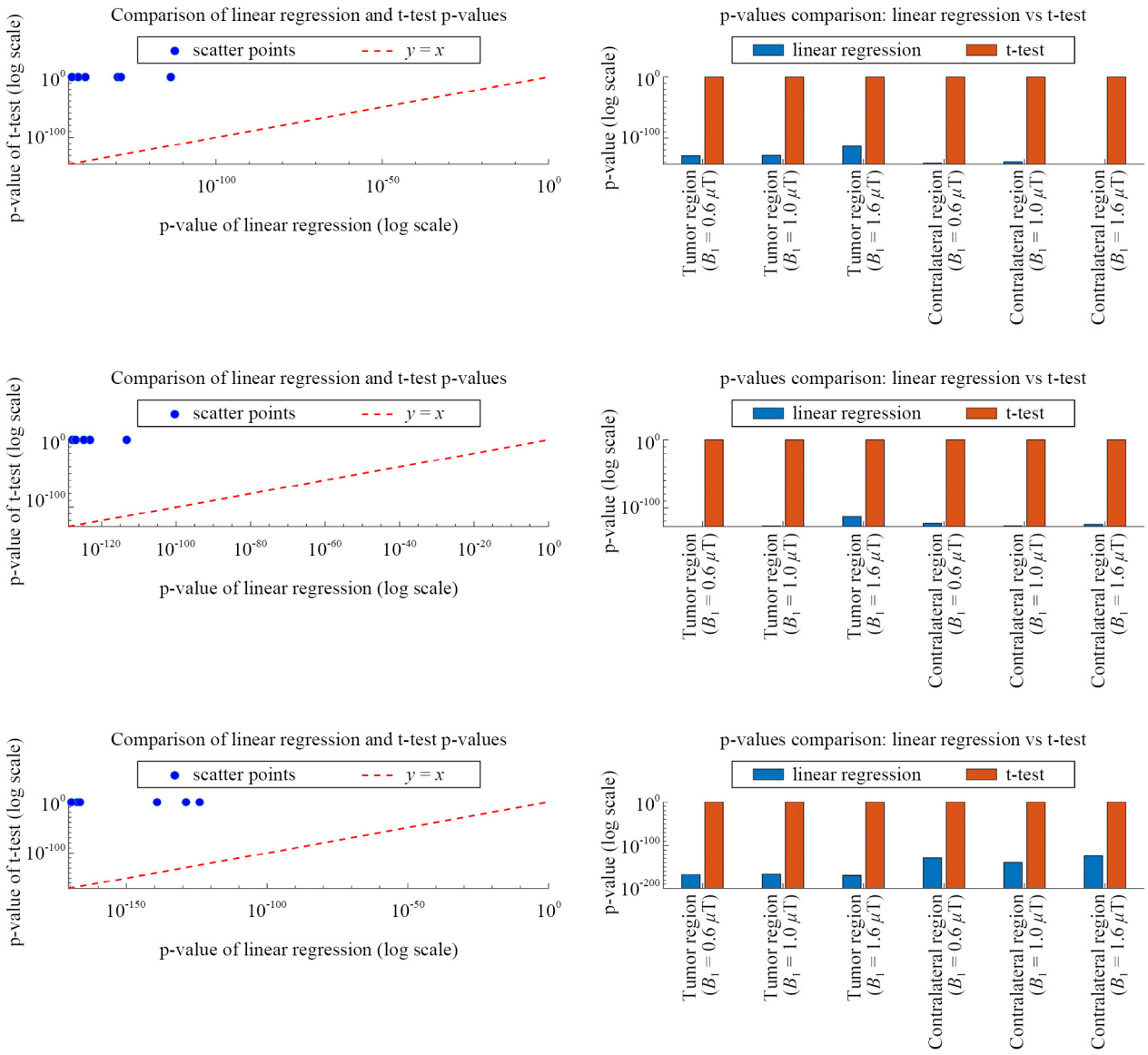

Figure 6. Results of t-tests comparing Z-spectra fitting results obtained with different numbers of starting points (all p-values > 0.05). The first, second, and third rows correspond to the comparison results between different numbers of starting points, namely 50 vs. 100, 50 vs. 1000, and 100 vs. 1000, respectively

In this section, linear regression analysis and statistical significance testing were performed on the Z-spectra fitting results obtained using the MS algorithm with 50, 100, and 1000 starting points, without SVD denoising. Figure 5 presents the linear regression results for different numbers of starting points under various B_1 values ($B_1 = 0.6\ \mu$T, 1.0 μT, and 1.6 μT) in both the tumor region and the contralateral region. The results demonstrate a high degree of consistency across different starting point numbers, indicating that the proposed method exhibits strong robustness and is largely insensitive to the number of starting points. Based on the analysis shown in Figure 5, t-tests were further conducted, as illustrated in

Figure 6. The statistical results show that all p-values are greater than 0.05, indicating that no significant differences exist among the Z-spectra fitting results obtained with different numbers of starting points. The corresponding results of the MS algorithm with SVD denoising are illustrated in Figure A5 and Figure A6 of Appendix.

5. Discussion

In this study, we propose a multi-start (MS) optimization framework for solving the global optimization problem of multi-pool R_{ex}-line-fit in CEST imaging. By upgrading the R_{ex}-line-fit solver from a single-start local optimization strategy to a global search framework, the proposed method improves the stability, robustness, and reproducibility of quantitative CEST parameter estimation under noisy and highly non-convex conditions. Given that local optima and initialization sensitivity are major challenges in in vivo CEST quantification, the present work provides both methodological and practical advances. The main implications are discussed below.

5.1 *Advantages of the multi-start algorithm in CEST parameter fitting*

A key contribution of this study lies in replacing the single-start trust-region-reflective (TRR) strategy used in our previous work (Sci Rep, 2024) with a multi-start global optimization framework. While TRR is computationally efficient under the analytical Rex formulation, it remains a local optimizer and is therefore sensitive to initialization, especially in multi-pool, multi-parameter, and noisy settings where the error surface is strongly non-convex.

The MS framework addresses this limitation by performing repeated local optimizations from multiple independent starting points sampled within predefined parameter bounds, followed by a global selection of the solution with the minimum residual. From an optimization perspective, this strategy effectively samples multiple basins of attraction in the parameter space. As noise increases the roughness of the objective function and the number of local minima, the probability that at least one starting point converges to the basin near the global optimum increases monotonically with the number of starts, following

$$1-(1-p)^N,$$

where p denotes the probability that a single initialization reaches the global basin and N is the number of starting points.

This theoretical expectation is directly supported by our experimental results. Through two validation experiments—with and without SVD-based denoising—and three initialization configurations (50, 100, and 1000 starts), we demonstrate that:

(i) the proposed MS-Rex framework yields comparable RMSE values under different noise levels, indicating robustness against noise; and

(ii) the fitting results are largely insensitive to the number of starting points once a moderate coverage of the parameter space is achieved.

Furthermore, linear regression analysis and statistical significance testing on in vivo data (Figures 5 and 6), as well as the corresponding SVD-denoised results (Figures A5–A6), show no statistically significant differences (all $p > 0.05$) among different initialization sizes across multiple B_1conditions and tissue regions. These results collectively demonstrate that the MS algorithm substantially reduces initialization dependence and improves the reproducibility of Rex-based CEST quantification.

Compared with other global optimization methods such as genetic algorithms (GA), particle swarm optimization (PSO), or grid search (GS), the MS framework achieves a favorable balance between global exploration and computational efficiency. Importantly, it leverages efficient local solvers rather than population-based evolution, which explains its superior speed while maintaining robustness.

5.2 *Advantages and scope of the Rex method for CEST quantification*

Another important factor contributing to the overall efficiency of the proposed framework is the use of R_{ex}-line-fit instead of full numerical Bloch-McConnell (BM) fitting. Unlike BM-based approaches, which require repeated numerical integration of coupled differential equations and involve a large number of strongly coupled parameters, the Rex formulation provides an analytical or semi-analytical description of exchange effects.

This leads to several advantages. First, the computational cost of a single model evaluation is greatly reduced, as no numerical solution of the Bloch-McConnell equations or matrix exponentials is required. Second, the number of free parameters to be estimated is reduced by fixing or prescribing certain quantities (e.g., chemical shifts), thereby lowering the dimensionality of the optimization problem and improving parameter stability. Third, the Rex parameter is primarily sensitive to solute concentration, exchange rate, and transverse relaxation time, while being less affected by non-specific tissue parameters, which enhances specificity in complex in vivo environments.

It should be clarified that Eq. (1) in this work explicitly includes the saturation time and therefore does not rely on a strict steady-state assumption. Instead, it describes the evolution of Z-magnetization under finite saturation. Nevertheless, limitations remain. In fast-exchange regimes or strongly coupled multi-pool systems, the analytical Rex approximation may not fully capture all exchange dynamics, potentially introducing bias. Similarly, under non-ideal saturation conditions—such as insufficient saturation time or severe B_1 inhomogeneity—the validity of the model assumptions may be reduced.

In such scenarios, the proposed MS-R_{ex} framework can serve as a robust and computationally efficient tool for initial estimation or rapid screening, which may subsequently be refined using non-steady-state qCEST, Ω-plot analysis, or full Bloch-McConnell simulations. Future work will focus on extending the current framework to larger cohorts and more complex exchange models, as well as integrating R_{ex}-based fitting with complementary quantification approaches to further enhance accuracy and applicability.

Author contributions

G.X: Conceptualization, Methodology, Software; Z.C: Data curation, Formal analysis, Investigation, Writing—original draft; T.-T.N: Data curation, Formal analysis; C.-Y.Z: Data curation, Resources; Y.-H.L: Investigation, Resources; R.-H.W: Funding acquisition, Project administration, Writing—review & editing; X.-L.Z: Methodology, Formal analysis, Investigation, Validation, Visualization, Writing—original draft.

Acknowledgments

The study was supported by the National Natural Science Foundation of China (Grant/Award Number: 82471974, 82411540241, 82020108016), the Medical Scientific Research Foundation of Guangdong Province (Grant/Award Numbers: B2025236, B2025782), the Medical Health Science and Technology Project of Shantou (Grant/Award Number: 220518156491349, 240428166497960), and the 2021 Grant for Key Science Technology and Innovation Project under the Guangdong Jieyang Development Program (Grant/Award Number: 210517084612609).

Ethics approval and consent to participate

All animal experiments are approved by the Ethics Committee of Shantou University Medical College (Approval ID: SUMCXM2024-452; Date: 2024 Nov 27) and conducted in accordance with the ARRIVE guidelines.

Availability of data and material

The data and material used and/or analysed during the current study are available from the corresponding author on reasonable request.

Conflict of interest

The authors declare no competing financial interest.

References

[1] Mennecke A, Khakzar KM, German A, Herz K, Fabian MS, Liebert A, et al. 7 tricks for 7 T CEST: improving the reproducibility of multipool evaluation provides insights into the effects of age and the early stages of Parkinson's disease. *NMR in Biomedicine*. 2023; 36(6): e4717. Available from: https://doi.org/10.1002/nbm.4717.

[2] Tang H, Wang S, Lai S, Chen Y, Yang W, Xiao G. Quasi-steady-state CEST prediction based on TCN-LSTM. *IEEE Access*. 2023; 11: 98765–98778. Available from: https://doi.org/10.1109/ACCESS.2023.3311711.

[3] Xiao G, Zhang X, Tang H, Huang W, Chen Y, Zhuang C, et al. Deep learning for dense Z-spectra reconstruction from CEST images at sparse frequency offsets. *Frontiers in Neuroscience*. 2023; 17: 1323131. Available from: https://doi.org/10.3389/fnins.2023.1323131.

[4] Xiao G, Zhang X, Yang G, Jia Y, Yan G, Wu R. Deep learning to reconstruct quasi-steady-state chemical exchange saturation transfer from a non-steady-state experiment. *NMR in Biomedicine*. 2023; 37(2): e4940. Available from: https://doi.org/10.1002/nbm.4940.

[5] Yang W, Zou J, Zhang X, Chen Y, Tang H, Xiao G, et al. An end-to-end LSTM-Attention based framework for quasi-steady-state CEST prediction. *Frontiers in Neuroscience*. 2023; 17: 1281809. Available from: https://doi.org/10.3389/fnins.2023.1281809.

[6] Zaiss M, Jin T, Kim SG, Gochberg DF. Theory of chemical exchange saturation transfer MRI in the context of different magnetic fields. *NMR in Biomedicine*. 2023; 36(6): e4961. Available from: https://doi.org/10.1002/nbm.4961.

[7] Perlman O, Zhu B, Zaiss M, Rosen MS, Farrar CT. An end-to-end AI-based framework for automated discovery of rapid CEST/MT MRI acquisition protocols and molecular parameter quantification (AutoCEST). *Magnetic Resonance in Medicine*. 2022; 87(6): 2792–2810. Available from: https://doi.org/10.1002/mrm.29173.

[8] Xiao G, Zhang XL, Wang SQ, Lai SX, Nie TT, Chen YW, et al. Quantitative separation of CEST effect by R(ex)-line-fit analysis of Z-spectra. *Scientific Reports*. 2024; 14(1): 21471. Available from: https://doi.org/10.1038/s41598-024-72141-4.

[9] Shah SM, Mougin OE, Carradus AJ, Geades N, Dury R, Morley W, et al. The z-spectrum from human blood at 7T. *NeuroImage*. 2018; 167: 31–40. Available from: https://doi.org/10.1016/j.neuroimage.2017.10.053.

[10] Wen Q, Wang K, Zhang Z, Hsu YC, Xu Y, Sun Y, et al. Chemical exchange saturation transfer imaging for epilepsy secondary to tuberous sclerosis complex at 3 T: optimization and analysis. *NMR in Biomedicine*. 2021; 34(9): e4563. Available from: https://doi.org/10.1002/nbm.4563.

[11] Carradus AJ, Bradley JM, Gowland PA, Mougin OE. Measuring chemical exchange saturation transfer exchange rates in the human brain using a particle swarm optimisation algorithm. *NMR in Biomedicine*. 2023; 36(11): e5001. Available from: https://doi.org/10.1002/nbm.5001.

[12] Martí R. Multi-start methods. In: Glover F, Kochenberger GA. (eds.) *Handbook of Metaheuristics*. Boston, MA: Springer US; 2003. p.355–368. Available from: https://doi.org/10.1007/0-306-48056-5_12.

[13] Martí R, Resende MG, Ribeiro CC. Multi-start methods for combinatorial optimization. *European Journal of Operational Research*. 2013; 226(1): 1–8. Available from: https://doi.org/10.1016/j.ejor.2012.10.012.

[14] Zaiss M, Bachert P. Chemical exchange saturation transfer (CEST) and MR Z-spectroscopy in vivo: a review of theoretical approaches and methods. *Physics in Medicine and Biology*. 2013; 58(22): R221. Available from: https://doi.org/10.1088/0031-9155/58/22/R221.

[15] Chen L, Barker PB, Weiss RG, van Zijl PCM, Xu J. Creatine and phosphocreatine mapping of mouse skeletal muscle by a polynomial and Lorentzian line-shape fitting CEST method. *Magnetic Resonance in Medicine*. 2019; 81(1): 69–78. Available from: https://doi.org/10.1002/mrm.27514.

[16] Cui J, Zhao Y, Sun C, Xu J, Zu Z. Evaluation of contributors to amide proton transfer-weighted imaging and nuclear Overhauser enhancement-weighted imaging contrast in tumors at a high magnetic field. *Magnetic Resonance in Medicine*. 2023; 90(2): 596–614. Available from: https://doi.org/10.1002/mrm.29675.

[17] Mirjalili S. Genetic algorithm. In: *Evolutionary Algorithms and Neural Networks: Theory and Applications*. Cham: Springer International Publishing; 2019. p.43–55. Available from: https://doi.org/10.1007/978-3-319-93025-1_4.

[18] Marini F, Walczak B. Particle swarm optimization (PSO): a tutorial. *Chemometrics and Intelligent Laboratory Systems*. 2015; 149: 153–165. Available from: https://doi.org/10.1016/j.chemolab.2015.08.020.

[19] Ugray Z, Lasdon L, Plummer J, Glover F, Kelly J, Martí R. Scatter search and local NLP solvers: a multistart framework for global optimization. *INFORMS Journal on Computing*. 2007; 19(3): 328–340. Available from: https://doi.org/10.1287/ijoc.1060.0175.

Appendix. The MR imaging of Sprague-Dawley rats

For our study, 8-week-old male Sprague Dawley (SD) rats (Beijing Vital River Laboratory Animal Technology Co., Ltd.) each weighing 250 g are used to create a tumor-bearing model. A 10 μL suspension of rat glioma C6 cells (approximately 2×10^6 cells) was implanted into the right basal ganglia (specific injection position: AP+1, ML+3, DV-5) of the rats using a Hamilton syringe and a 30-gauge needle. Two weeks after the tumor cell implantation, the rats were subjected to MRI. Rats were anesthetized with isoflurane mixed with O_2 at a rate of 1 L/min; 4.0% isoflurane was used for anesthesia induction, and 2.0%–3.0% isoflurane was used for maintenance. A respiratory probe was used to monitor the breath rate throughout the MRI experiments. The respiration rate and body temperature during the scan in 7 T were 60–70 times/min and 38.5–39.5 °C, respectively.

MRI was performed using a 7 T horizontal bore small animal MRI scanner (Agilent Technologies, Santa Clara, CA, U.S.A.) with a surface coil (Timemedical Technologies, China) for transmission and reception. The rat was positioned to ensure that the tumor was centered on the magnetic field. Imaging parameters were as follows: repetition time (TR) = 6000 ms, echo time (TE) = 40 ms, array = frequency offsets, slice thickness = 2 mm, field of view (FOV) = 64 × 64 mm, matrix size = 64 × 64, spatial resolution = 1×1 mm, averages = 1. An echo planar imaging (EPI) readout sequence was used to obtain CEST images, where continuous wave (CW) radio-frequency (RF) irradiation was implemented on scanners. The saturation times was 5.0 s, with 49 frequency offsets evenly distributed from −6 to 6 ppm relative to the resonance of water.

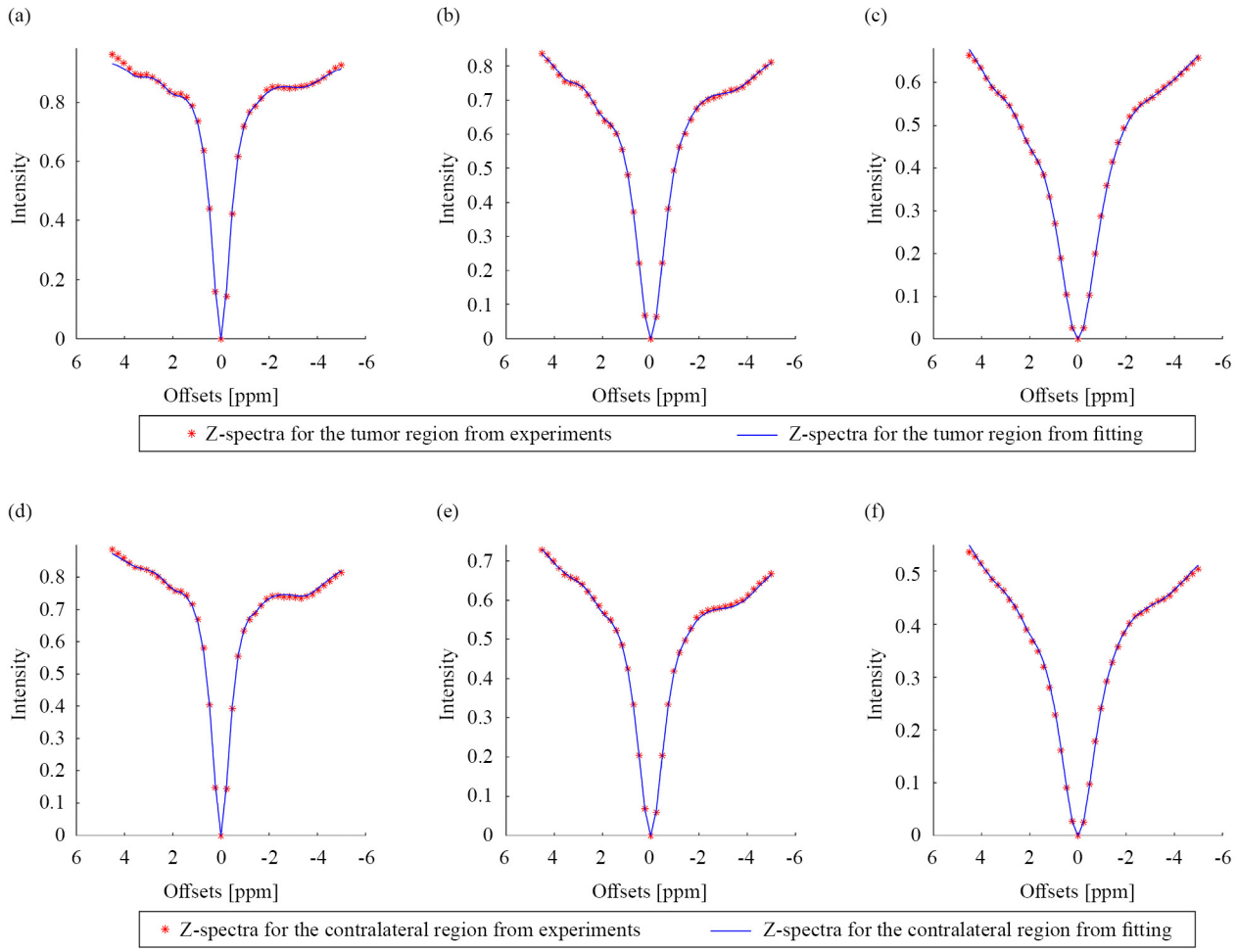

Figure A1. Z-spectra fitting from the tumor region and the contralateral region using the R_{ex}-line-fit when it is solved by MS using 50 starting points without SVD denoising. (a) $B_1 = 0.6$ μT for the tumor region, (b) $B_1 = 1.0$ μT for the tumor region, (c) $B_1 = 1.6$ μT for the tumor region, (d) $B_1 = 0.6$ μT for the contralateral region, (e) $B_1 = 1.0$ μT for the contralateral region, (f) $B_1 = 1.6$ μT for the contralateral region

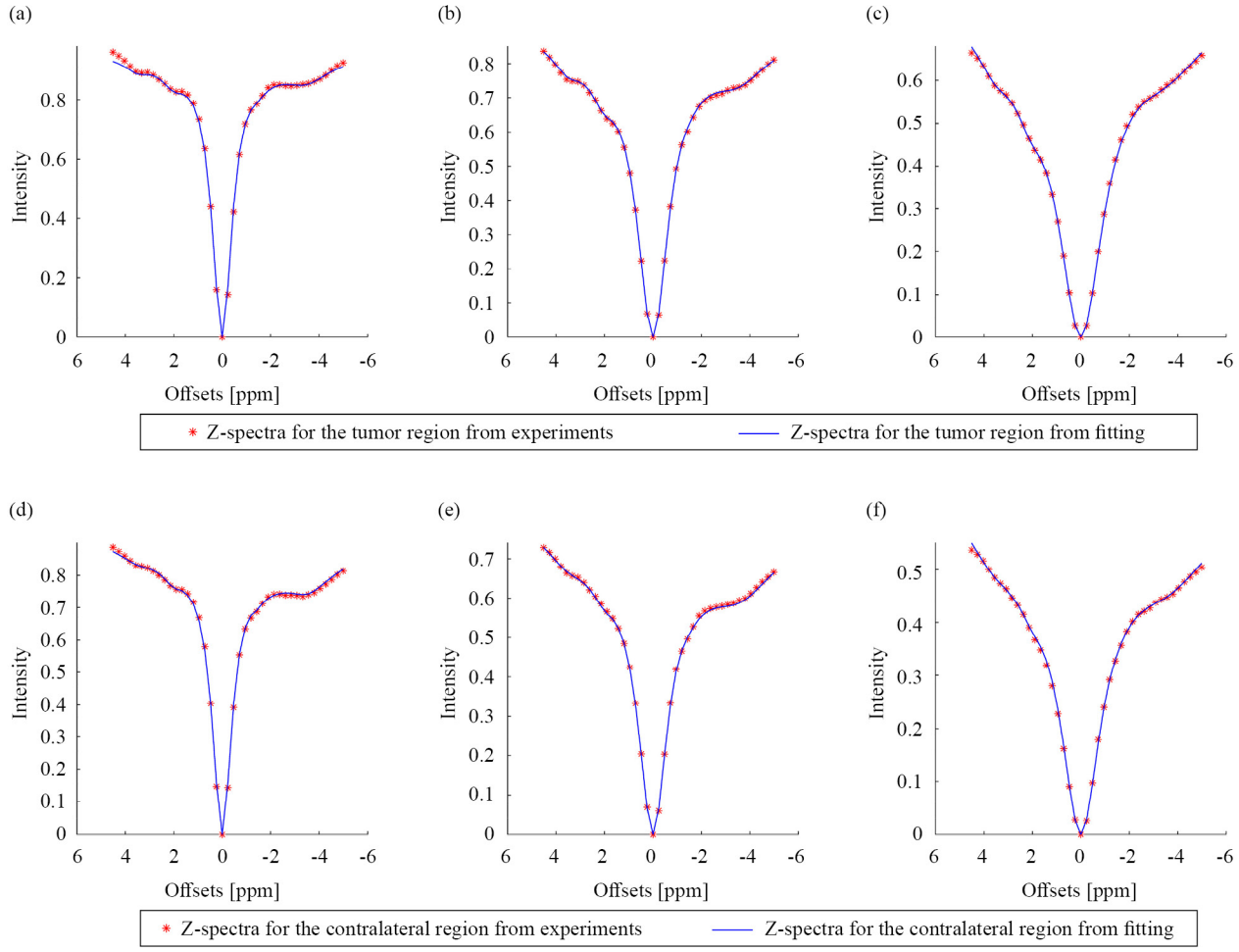

Figure A2. Z-spectra fitting from the tumor region and the contralateral region using the R_{ex}-line-fit when it is solved by MS using 100 starting points without SVD denoising. (a) $B_1 = 0.6\ \mu$T for the tumor region, (b) $B_1 = 1.0\ \mu$T for the tumor region, (c) $B_1 = 1.6\ \mu$T for the tumor region, (d) $B_1 = 0.6\ \mu$T for the contralateral region, (e) $B_1 = 1.0\ \mu$T for the contralateral region, (f) $B_1 = 1.6\ \mu$T for the contralateral region

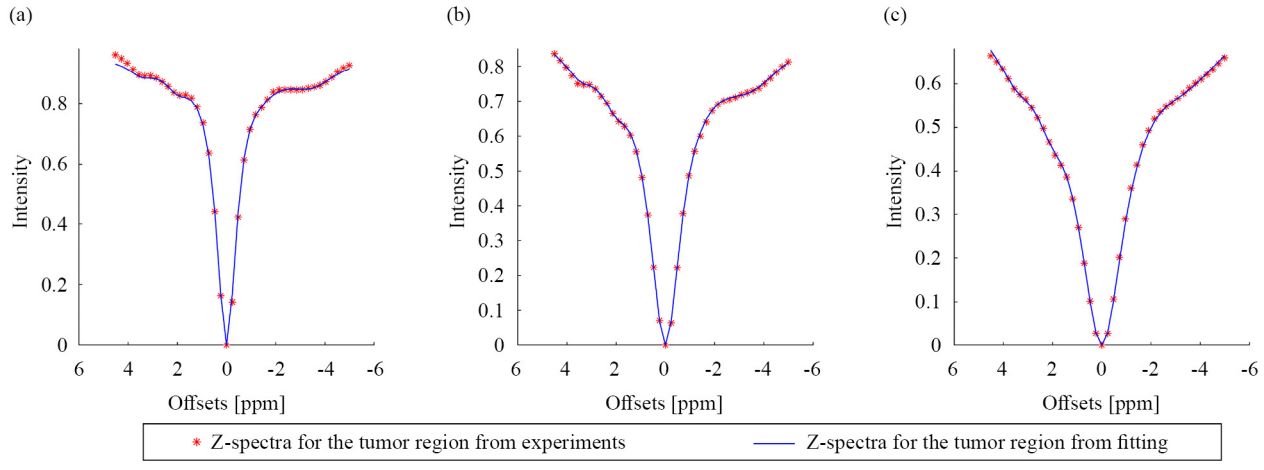

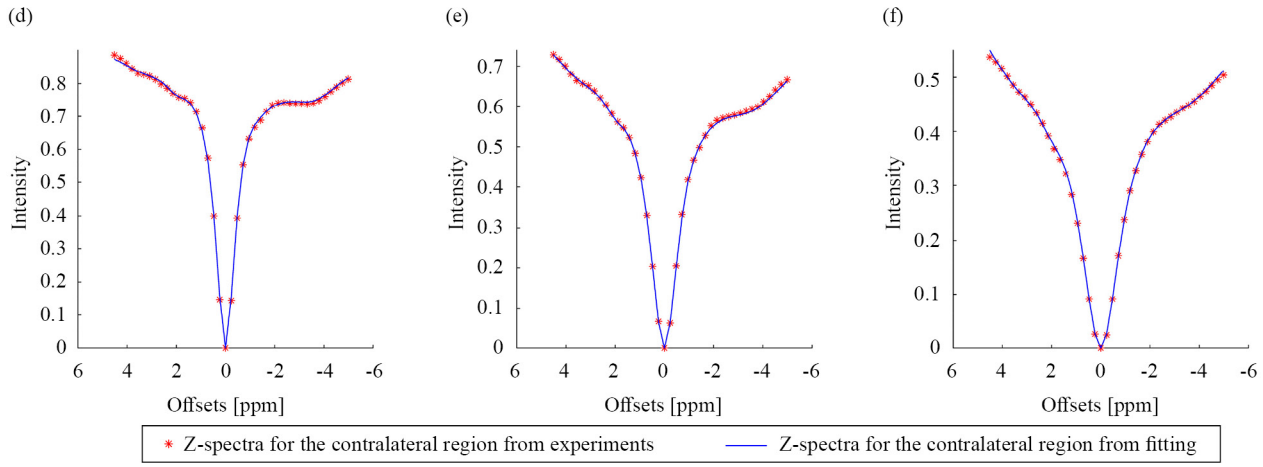

Figure A3. Z-spectra fitting from the tumor region and the contralateral region using the R_{ex}-line-fit when it is solved by MS using 50 starting points with SVD denoising. (a) $B_1 = 0.6\ \mu$T for the tumor region, (b) $B_1 = 1.0\ \mu$T for the tumor region, (c) $B_1 = 1.6\ \mu$T for the tumor region, (d) $B_1 = 0.6\ \mu$T for the contralateral region, (e) $B_1 = 1.0\ \mu$T for the contralateral region, (f) $B_1 = 1.6\ \mu$T for the contralateral region

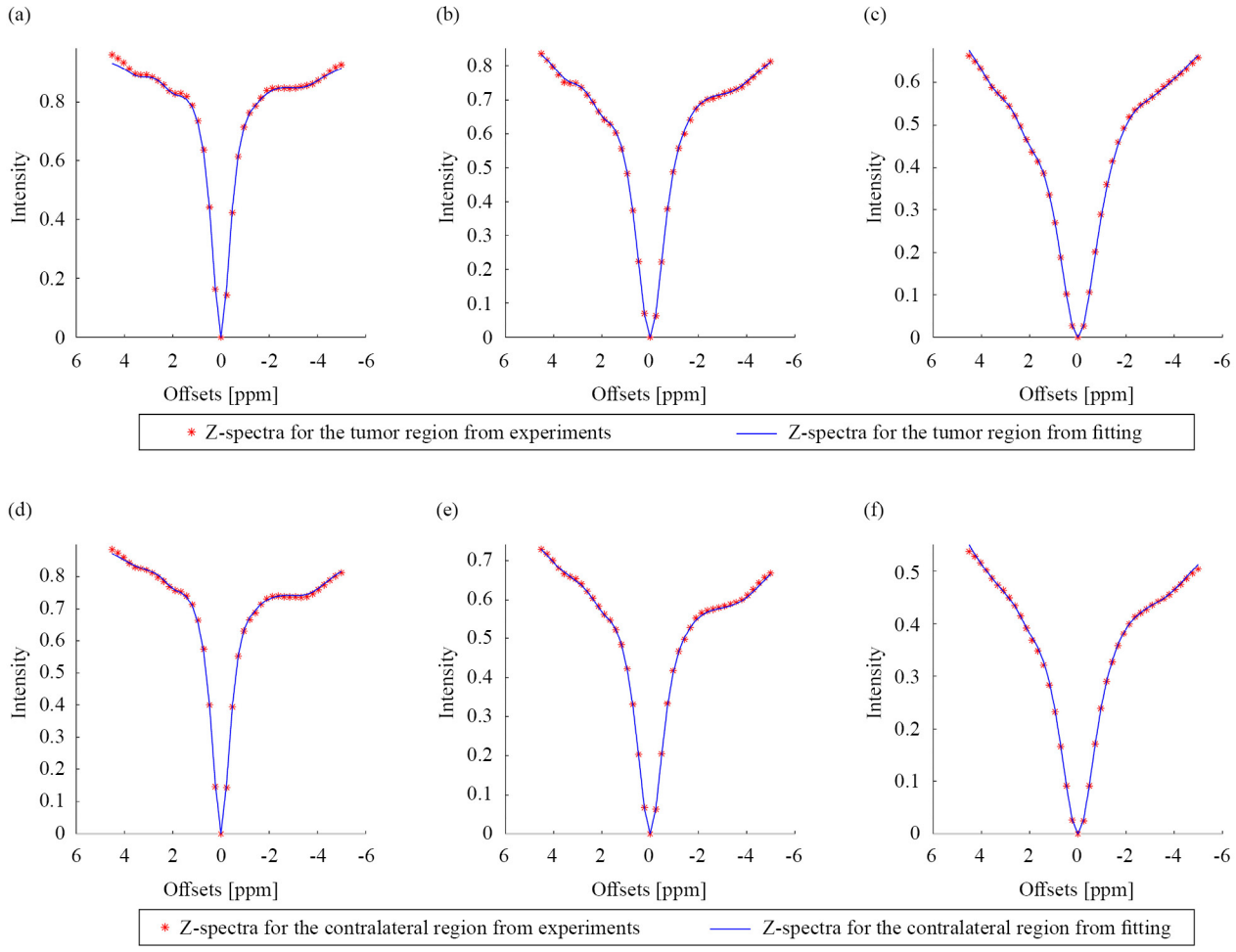

Figure A4. Z-spectra fitting from the tumor region and the contralateral region using the R_{ex}-line-fit when it is solved by MS using 100 starting points with SVD denoising. (a) $B_1 = 0.6\ \mu$T for the tumor region, (b) $B_1 = 1.0\ \mu$T for the tumor region, (c) $B_1 = 1.6\ \mu$T for the tumor region, (d) $B_1 = 0.6\ \mu$T for the contralateral region, (e) $B_1 = 1.0\ \mu$T for the contralateral region, (f) $B_1 = 1.6\ \mu$T for the contralateral region

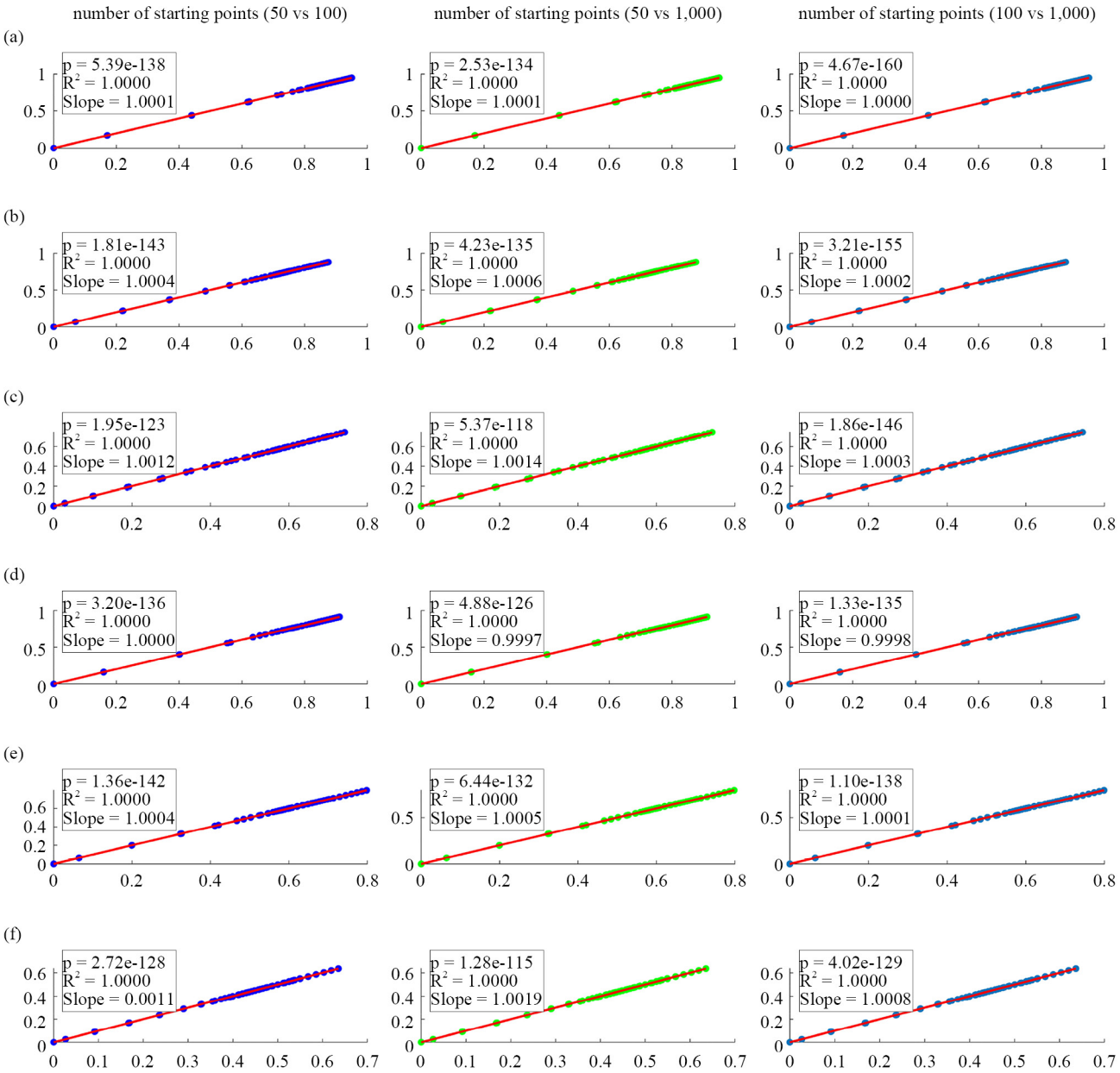

Figure A5. Linear regression analysis of Z-spectra fitting results obtained with different numbers of starting points (50, 100, and 1000) and B_1 values (0.6 μT, 1.0 μT, and 1.6 μT) in the tumor and contralateral regions, with SVD denoising. (a) $B_1 = 0.6$ μT for the tumor region; (b) $B_1 = 1.0$ μT for the tumor region; (c) $B_1 = 1.6$ μT for the tumor region; (d) $B_1 = 0.6$ μT for the contralateral region; (e) $B_1 = 1.0$ μT for the contralateral region; (f) $B_1 = 1.6$ μT for the contralateral region

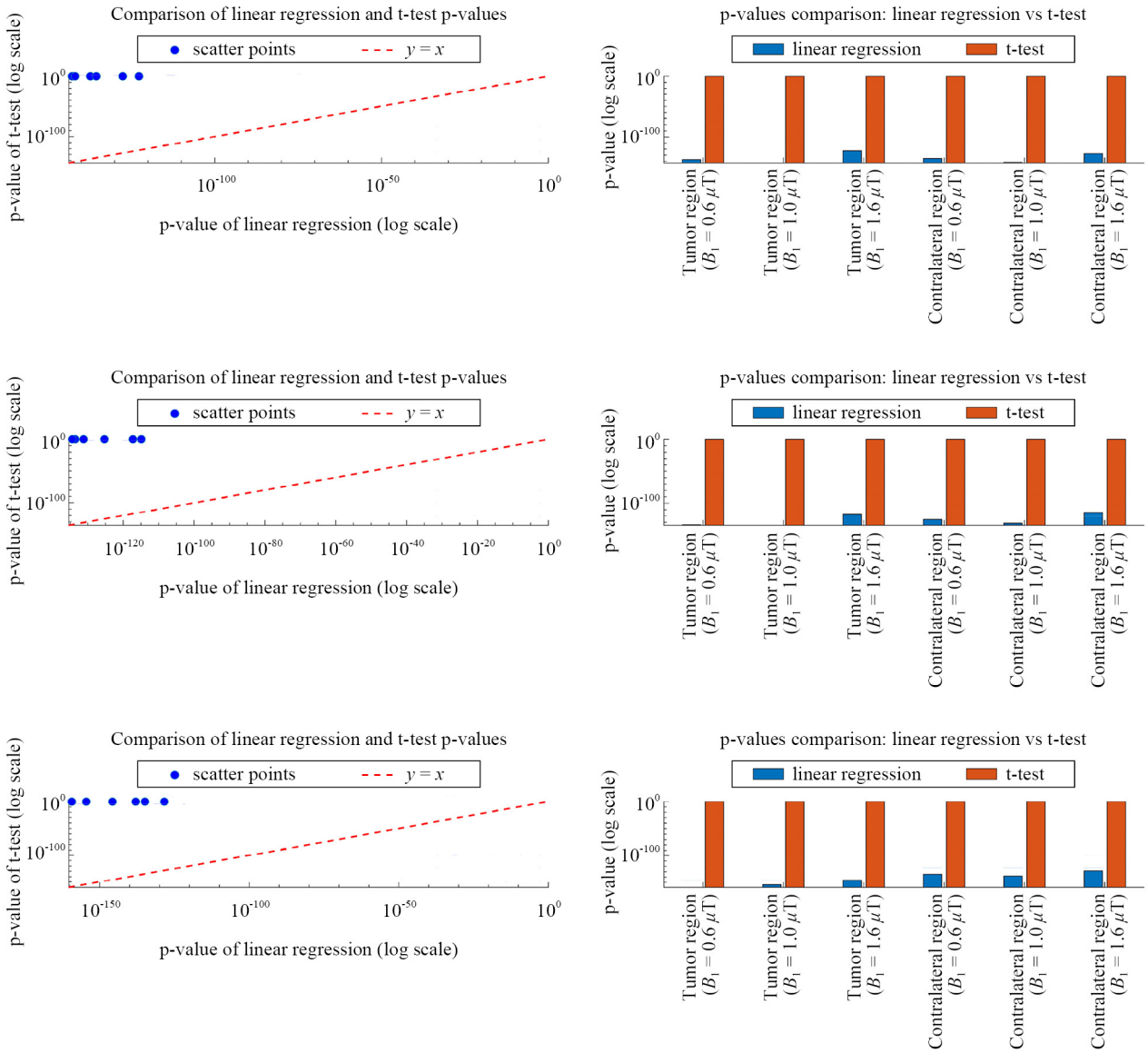

Figure A6. Results of *t*-tests comparing Z-spectra fitting results obtained with different numbers of starting points, with SVD denoising (all *p*-values > 0.05). The first, second, and third rows correspond to the comparison results between different numbers of starting points, namely 50 vs. 100, 50 vs. 1000, and 100 vs. 1000, respectively